ACS APPLIED MATERIALS & INTERFACES

Influence of Ti^{4+} on the Electrochemical Performance of Li-Rich Layered Oxides - High Power and Long Cycle Life of $Li_2Ru_{1-x}Ti_xO_3$ Cathodes

Abdul Kareem Kalathil,[†,∥] Paulraj Arunkumar,[†,∥] Da Hye Kim,[‡] Jong-Won Lee,[§] and Won Bin Im*[,†]

[†]School of Materials Science and Engineering, Chonnam National University, 300 Yongbong-dong, Buk-gu, Gwangju, 500-757, Republic of Korea

[‡]Ultimate Manufacturing Technology R&BD Group, KITECH, Cheonan, 331-822, Republic of Korea

[§]New and Renewable Energy Research Division, Korea Institute of Energy Research, Daejeon, 305-343, Republic of Korea

Supporting Information

ABSTRACT: Li-rich layered oxides are the most attractive cathodes for lithium-ion batteries due to their high capacity (>250 mAh g^{-1}). However, their application in electric vehicles is hampered by low power density and poor cycle life. To address these, layered $Li_2Ru_{0.75}Ti_{0.25}O_3$ (LRTO) was synthesized and the influence of electroinactive Ti^{4+} on the electrochemical performance of Li_2RuO_3 was investigated. LRTO exhibited a reversible capacity of 240 mAh g^{-1} under 14.3 mA g^{-1} with 0.11 mol of Li loss after 100 cycles compared to 0.22 mol of Li for $Li_2Ru_{0.75}Sn_{0.25}O_3$. More Li^+ can be extracted from LRTO (0.96 mol of Li) even after 250 cycles at 143 mA g^{-1} than Li_2RuO_3 (0.79 mol of Li). High reversible Li extraction and long cycle life were attributed to structural stability of the Li*M*$_2$ layer in the presence of Ti^{4+}, facilitating the lithium diffusion kinetics. The versatility of the Li_2MO_3 structure may initiate exploration of Ti-based Li-rich layered oxides for vehicular applications.

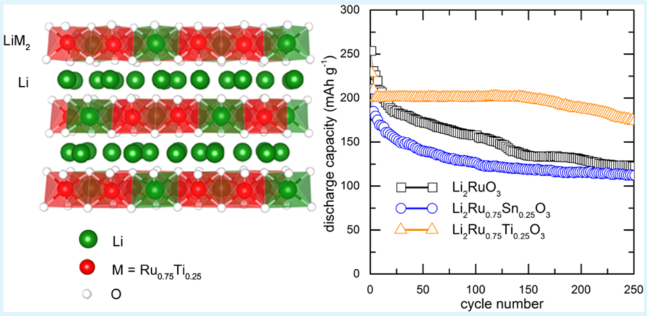

KEYWORDS: *Li-rich layered oxides, Li_2RuO_3, cathodes, cycle life, and power density*

■ INTRODUCTION

The rechargeable lithium-ion battery has dominated the electronic industry owing to its high energy density and is considered as the promising power sources for electric vehicles.[1] The current lithium-ion batteries still have insufficient energy density for vehicular applications and need new advancements in the performance, safety, and cost that requires a deep understanding of the mechanisms of high capacity intercalation electrodes and development of new efficient and cost-effective materials.[2] Several high capacity cathodes were explored in commercial scale, explicitly olivine ($LiFePO_4$),[3] spinels ($LiNi_{0.5}Mn_{1.5}O_4$),[4] and layered oxides ($LiCoO_2$,[5] $LiCo_{0.33}Ni_{0.33}Mn_{0.33}O_2$).[6] However, the attainable rechargeable capacity of these cathodes approaches the limits of 120−200 mAh g^{-1}, with the highest capacity obtained for the layered oxides. In the search for new cathodes with enhanced capacity (∼300 mAh g^{-1}), layered oxides with excess lithium (known as lithium-rich layered oxides) were reported and had received greater interest due to their high energy density (1000 Wh kg^{-1}) and high capacities ≥ 280 mAh g^{-1} with wide operating voltages of 3−4.6 V.[7,8]

These materials are typical solid solution described by two different notations: $xLi_2MnO_3\cdot(1-x)LiMO_2$ (M = Mn, Ni, Co, Fe, Cr, etc.),[8] a solid solution of two layered structures, $LiMO_2$ and Li_2MnO_3, or as a single component, $Li[Li_{1/3}Mn_{2/3-x}M_x]O_2$.[9] Although they have high capacity, they face many challenges that include low initial Coulombic efficiency, poor rate capability, voltage decay during cycling, and poor cycle life, which are to be overcome to realize their utilization in commercial lithium-ion batteries.[8] The solid solution was formed by the similarity in the structure of layered $LiMO_2$ possessing a transition metal (M) layer (with MO_6 symmetry) in which lithium is occupying the sites in between the layers. If $^1/_3$ of the M are replaced by Li from the layered $LiMO_2$ phase, forming a LiM_2 layer, it replicates the Li_2MO_3 structure, resulting in the $Li(Li_{1/3}M_{2/3})O_2$ phase.[10] The LiM_2 layer forms a honeycomb structure in which lithium ions are surrounded by six transition metals.[11] Li_2MO_3 materials crystallize in space groups, namely, $C2/c$ (M = Ru, Ti, Zr)[12−14] or $C2/m$ (M = Mn, Sn, Ir, Rh)[15−18] or $P3_112$ (Pt)[19] or $R3m$ (Mo)[20] monoclinic cells, while the stacking of LiM_2 layers is dependent on the nature of the (M) transition metal,[17] which may determine the electrochemical performance of the electrode. The role of stacking order of LiM_2 layers in Li_2MO_3 structures on the

Received: November 12, 2014
Accepted: March 11, 2015
Published: March 11, 2015

DOI: 10.1021/am507951x

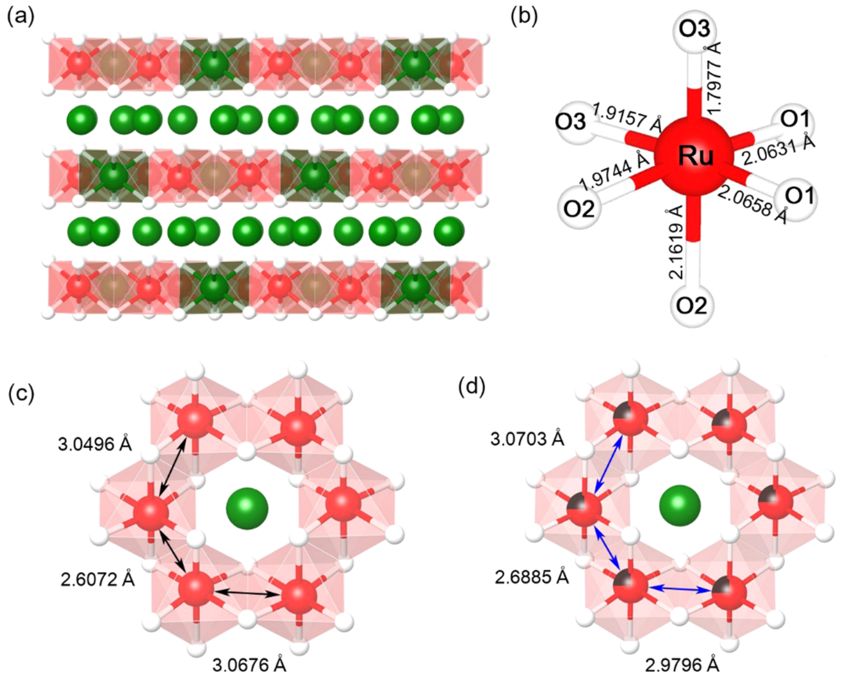

Figure 1. Crystal structural representations of (a) layered Li_2RuO_3 and (b) its Ru octahedral site, and LiM_2 layer depicting the transition metal hexagonal framework of (b) Li_2RuO_3 and (c) $Li_2Ru_{0.75}Ti_{0.25}O_3$ with Ru, Ti, Li, and O atoms in red, black, green, and white, respectively.

electrochemical performances was unclear. Few groups have claimed that the decrease in the stacking order/increase in the stacking faults results in improving the discharge capacity due to enhanced surface area caused by these defects/stacking faults.[21,22] However, these stacking faults, which are actually a shift in the LiM_2 layers from one layer to the other, would affect the lithium insertion/extraction apart from the increase in surface area. On the basis of thermodynamics, highly ordered materials that are devoid of defects/stacking faults have the lowest energy state, thereby reducing the activation energy barrier for the lithium diffusion. Hence, structural rigidity with higher stacking of transition metal layers would improve the diffusion kinetics of lithium ions.

The core issues of Li-rich layered cathodes are the capacity loss, poor cycle life, and increased cell resistance upon cycling. In an attempt to mitigate few of the above-mentioned issues, few research groups focused to incorporate an electroinactive element into Li-rich layered oxides and understand its role on the electrochemical performance of these cathodes. Sathiya et al.[23] explored the effect of Sn doping on the electrochemical properties of Li-rich layered oxides (Li_2MO_3, M = Ru) and reported the enhanced cyclability and reduced voltage decay in the presence of electrochemically inactive isovalent Sn^{4+} ions. However, the cyclability and electrochemical propeties were not much improved due to the stacking fault observed in the transition metal (LiM_2) layer of $Li_2M_{1-x}Sn_xO_3$ (M = Ru), which is a typical phenomenon observed in the Sn-based layered oxides, Li_2SnO_3.[16] Hence, in pursuit of improving the performance of Li-rich layered oxides, we report a $Li_2Ru_{1-x}Ti_xO_3$ cathode with a single redox cation to explore the influence of Ti^{4+} on the electrochemical properties that include power density and cycle life. Ti doping is expected to possibly favor the reversible lithium extraction with negligible structural change and to improve the cyclability of the electrode. Moreover, the Ti−O bond, which is stronger than the Ru−O bond, tends to stabilize the crystal structure of Li_2RuO_3 and thereby enhances its electrochemical performance, as evidenced in layered-type $LiM_{1-x}Ti_xO_2$ (M = Ni, Mn) cathodes.[24,25] Recently, Sathiya et al.[26] have explored the Ti-doped Li_2RuO_3 cathode for understanding the origin of voltage decay at lower C rates (C/5 rate). However, the role of Ti on the discharge capacity of Li_2RuO_3 at high C rates were not explored with a wide potential window (2.0−4.8 V). In this paper, we have investigated the influence of Ti doping on the electrochemical performance of layered Li_2MO_3 oxides at higher C rates, with the focus on structural stability of the Li_2MO_3 structure. Single phase $Li_2Ru_{1-x}M_xO_3$ (M = Ti, Sn) cathodes were synthesized, and their electrochemical performance were investigated. This study may result in the fundamental understanding of the usage of electroinactive Ti^{4+} species in the Li-rich layered oxides that may contribute to the development of high capacity cathodes.

■ EXPERIMENTAL SECTION

Sample Preparation. Series of $Li_2Ru_{1-x}Ti_xO_3$ cathodes (x = 0, 0.10, 0.25, 0.40, 0.60, 0.80, and 1.00) and $Li_2Ru_{0.75}Sn_{0.25}O_3$ were prepared by solid-state reaction. All chemical reagents used in the experiments were analytical grade. Stoichiometric amounts of $Li(CH_3COO)_2$ (99.9%, Sigma-Aldrich), RuO_2 (99.9%, Kojundo Chemicals) and TiO_2 (99.5%, Sigma-Aldrich), or SnC_2O_4 (98%, Sigma-Aldrich) were homogenized, using a mortar and pestle with a 10 wt % excess of the stoichiometric amount of $Li(CH_3COO)_2$ to compensate for its volatilization at high temperature. The resultant mixture was heated in an alumina crucible at 1100 °C for 12 h with the heating rate of 2 °C min^{-1}.

Structural and Morphology Analysis. The phase identification of series of $Li_2Ru_{1-x}Ti_xO_3$ (x = 0 to 1.00) and $Li_2Ru_{0.75}Sn_{0.25}O_3$ cathodes were carried out using powder X-ray diffraction (XRD). The diffraction intensity data were collected using a Philips X'Pert diffractometer with Cu Kα radiation. Neutron powder diffraction data were collected at room temperature using a high-resolution powder diffractometer in the Hanaro Center of Korea Atomic Energy Research Institute, Republic of Korea. Neutron powder diffraction data were collected over an angle range of $0° \leq 2\theta \leq 160°$ at λ = 1.8348 Å

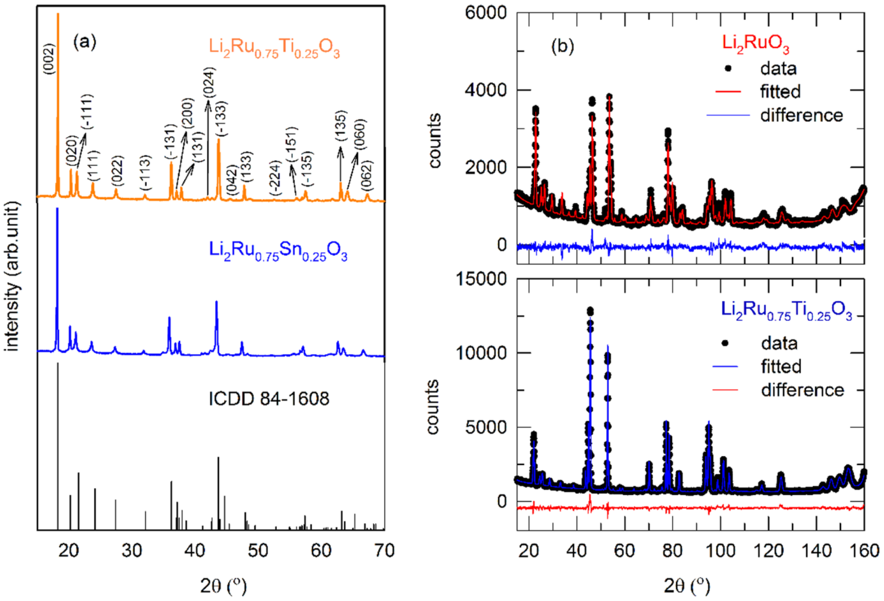

Figure 2. (a) XRD patterns of $Li_2Ru_{0.75}Sn_{0.25}O_3$ and $Li_2Ru_{0.75}Ti_{0.25}O_3$ indexed with standard Li_2RuO_3 with ICDD No. 84-1608 and space group: *C*2/*c*. (b) Neutron diffraction Rietveld refinement patterns of Li_2RuO_3 and $Li_2Ru_{0.75}Ti_{0.25}O_3$ with black dots representing the observed profile, and the line represents the fitted profile and difference profile (at the bottom).

(neutron), with 4 h of collection time. The Rietveld refinement was made with the General Structure Analysis System (GSAS) program.[27] Bond valence sums were calculated from the refined neutron diffraction results, to investigate the structural stability of the synthesized cathodes. The particle size and morphology were analyzed by field emission-scanning electron microscopy (FE-SEM) and high-resolution transmission electron microscopy (HR-TEM). The SEM images were obtained using a Hitachi S-4700, and TEM were recorded using an FEI Tecnai F20 at 200 kV, in the Korea Basic Science Institute (KBSI), Gwangju, Republic of Korea.

Electrochemical Characterization. The electrochemical properties of $Li_2Ru_{1-x}Ti_xO_3$ (x = 0−1.00) and $Li_2Ru_{0.75}Sn_{0.25}O_3$ cathodes were evaluated with lithium metal as the reference electrode. The two-electrode electrochemical cells were fabricated by using a mixture of active cathode material, conductive carbon (KETJEN black), and PTFE binder with a weight ratio of 75:10:15%. This mixture was pressed onto an aluminum mesh current collector and dried under vacuum at 120 °C for 12 h before cell assembling. The electrolyte was 1 mol/L $LiPF_6$ dissolved in a 1:1 mixture of ethylene carbonate (EC) and dimethyl-carbonate (DMC). A 2032 coin type cell was fabricated, which consists of a cathode and lithium metal anode separated by a polymer membrane and glass fiber, inside the glovebox filled with high-pure argon, and aged for 12 h before the electrochemical measurements.

The charge−discharge measurements were carried out using a NAGANO BTS-2004H battery charger between 2.0 and 4.8 V vs Li^+/Li. Cyclic voltammetry was measured with an Autolab electrochemical workstation at a scan rate of 0.1 mV s^{-1} between 2 and 4.8 V vs Li^+/Li. The electrochemical impedance spectroscopy (EIS) tests were performed using the Autolab electrochemical workstation with a voltage of 10 mV amplitude over a frequency range of 10^6 to 10^{-2} Hz.

Computational Methods. The calculations were performed with the end member, Li_2RuO_3, and then substituting Ru with transition metals, namely, Ti and Sn. The transition metals modeled are in their +4 state, which represents the chemical environment where oxygen loss occurs. All calculations were performed using the Vienna Ab initio Simulation Package (VASP).[28] The generalized gradient approximation (GGA) with the Perdew and Wang (PW91) potential was chosen to describe the exchange and correlation.[29] The plane-wave energy cutoff was set to 400 eV. A Monkhorst−Pack k-point mesh of 2 × 2 × 2 was set for energy calculations, and a 4 × 4 × 4 mesh was set for density of states (DOS) calculations. A 48-atom unit cell was fully relaxed using conjugate gradient energy minimization until the total energy changes were less than 1×10^{-5} eV. To correct the on-site Coulombic and exchange interaction of the localized Ti and Ru d electrons, we use the spin-polarized DFT+U approach. The effective Hubbard parameters ($U_{eff} = U - J$) are 4 and 4.2 eV for Ru[23] and Ti[30] atoms, respectively.

RESULTS AND DISCUSSION

Structural Characterization of Cathodes. The crystal structures of Li_2RuO_3 and $Li_2Ru_{0.75}Ti_{0.25}O_3$ were refined to expore the effect of Ti^{4+} doping in the Li_2RuO_3 structure and are depicted in Figure 1. The Li_2RuO_3 structure is composed of transition metal layers separated by a lithium layer in which oxygen forms the cubic close packing in the lattice. The transition metal layer consists of a mixture of Li^+ and Ru^{4+} ions in a 1:2 ratio ($LiRu_2$), and these ions occupy distorted octahedral sites, as depicted in Figure 1a,b, and are expressed as a $Li(Li_{1/3}Ru_{2/3})O_2$ layer, which is similar to the layered $LiMO_2$ structure. The $LiRu_2$ layers are composed of edge-sharing MO_6 octahedra that are arranged in a two-dimensional hexagonal network, in which lithium ions are surrounded by six RuO_6 and form honeycomb patterns, as shown in Figure 1c. Interestingly, Ru^{4+} makes quadruple bonds with neighboring Ru^{4+} in the honeycomb lattices of edge-shared RuO_6 layers and the Ru−Ru bonding in the layered oxide realizes good electronic and ionic conductivity. The Ru-containing layers are highly ordered to give a continuous hexagonal network of Ru^{4+} in alternate basal planes. The stacking sequence in this compound is “ABAB” along the c axis. The layered Li sites are nearly identical to the α-$NaFeO_2$ structure that might allow reversible lithium extraction with fast electrode kinetics. In the $Li_2Ru_{0.75}Ti_{0.25}O_3$, one in every four Ru^{4+} sites is replaced by Ti^{4+} (Figure 1d), in which the metal−metal quadruple bonds exist in the honeycomb lattice structure as similar to Li_2RuO_3. Ru and Ti form Ru^{4+}−Ti^{4+} quadruple bonds along with the Ru^{4+}−Ru^{4+} metal−metal bonds, thus, preventing any chance of drastic crystallographic change and thereby preserving the advantage of a layered structure and the metal−metal bond.[31] Three metal−

metal quadraple bonds exist in $Li_2Ru_{0.75}Ti_{0.25}O_3$, out of which two bonds correspond to Ru−Ru bonds, which are longer than the Ru−Ru bonds of Li_2RuO_3, while Ru−Ti (2.96 Å) is shorter than the Ru−Ru (3.06 Å) bonds in Li_2RuO_3 due to the higher electropositive nature of Ti than Ru, forming stronger Ru−Ti quadruple bonds in $Li_2Ru_{0.75}Ti_{0.25}O_3$ as derived from the neutron diffraction results.

X-ray diffraction (XRD) patterns of $Li_2Ru_{0.75}Ti_{0.25}O_3$ and $Li_2Ru_{0.75}Sn_{0.25}O_3$ obtained by the solid-state synthesis at 1100 °C are depicted in Figure 2a. The XRD patterns of $Li_2Ru_{1-x}Ti_xO_3$ cathodes with $x = 0.10$, 0.25, 0.40, 0.60, 0.80, and 1.00 are shown in Figure S1 of the Supporting Information. The diffraction patterns of all the cathodes were identified as the monoclinic Li_2RuO_3 structure of JCPDS no. 84-1608 with space group *C*2/*c*, as reported in previous literature.[12] No additional peaks are observed, revealing the high purity of the material, even though single step heating at 1100 °C was employed. The diffraction peaks were shifted toward higher Bragg's angle for $Li_2Ru_{0.75}Ti_{0.25}O_3$, which can be attributed to the smaller ionic radii of Ti^{4+} with 0.605 Å compared to Sn^{4+} and Ru^{4+} with ionic radii of 0.690 and 0.620 Å at the octahedral site, respectively.[32] The XRD peaks between Bragg's angles of 20° and 23° represent superlattice peaks that describe the stacking of the ordered transition metal layer along the monoclinic *c* axis of layered oxides.[33−35] These peaks are of specific importance to the local (nearest cation neighbor) environment of the lithium ion, since the peak intensities are attributed to the ordering of lithium, ruthenium, and other transition metal ions present in the transition metal layers.

Structural Rigidity of $Li_2Ru_{0.75}M_{0.25}O_3$ (*M* = Ti, Sn) Electrodes. Figure 2b shows the Rietveld refinement results of the neutron diffraction of Li_2RuO_3 and $Li_2Ru_{0.75}Ti_{0.25}O_3$. The refinement of Li_2RuO_3 and $Li_2Ru_{0.75}Ti_{0.25}O_3$ was performed using a monoclinic structure with *C*2/*c* space group. The calculated unit cell parameters of Li_2RuO_3 and $Li_2Ru_{0.75}Ti_{0.25}O_3$ are listed in Table 1, and their refined structural parameters are listed in Table S1 of the Supporting Information. The observed decrease in the unit cell parameters ("*b*" and "*c*") with the addition of Ti is a direct consequence of the smaller radii of Ti^{4+} (0.605 Å) as compared with those of Ru^{4+} (0.620 Å) with six coordination.[32] The stacking is slightly altered for $Li_2Ru_{0.75}Ti_{0.25}O_3$, where the "*a*" axis value was increased compared to pristine Li_2RuO_3. Ti-doped Li_2RuO_3 revealed higher stacking of the LiM_2 layers with lower full-width at half-maximum superlattice peaks compared to Sn samples. To ensure the structural rigidity of synthesized cathodes, bond valence sums (BVSs) were calculated for the individual metals and are depicted in Table 2. BVS calculations provide a reliable method of assigning formal oxidation states of an atom in a material from the bond parameters, which are correlated to the rigidity of the crystal structure.[36,37] Ru^{4+} in Li_2RuO_3 was bonded with BVS less than +4 (∼3.43), while Ru^{4+}/Ti^{4+} in $Li_2Ru_{0.75}Ti_{0.25}O_3$ was also under-bonded with 3.81. However, the Ti^{4+} doping in Li_2RuO_3 realizes in optimizing the bonding network and approaches BVS close to ideal valence of +4 (∼3.81). This would stabilize the crystal structure with high rigidity and improves the structural integrity of the Li_2MO_3 structures and can improve the electrochemical performance by facilitating electron transport and lithium diffusion kinetics.[35,38] Lithium extraction is more facile from a pure lithium layer, which is sandwiched between two transition metal layers than from the transition metal layer. Any change in the stacking of the LiM_2 layers would certainly affect the extraction of lithium from the pure Li layer. Hence, the structural stability and stacking of the LiM_2 layers would affect the initial Li extraction and the subsequent reversible lithium insertion/deinsertion process upon cycling for the improved electrochemcial performance that includes cycle life and power capability.

Table 1. Rietveld Refinement and Crystal Data from Neutron Diffraction

formula	Li_2RuO_3	$Li_2Ru_{0.75}Ti_{0.25}O_3$
radiation type	neutron	
T (K)	295	
2*θ* range (deg)	15−160	
symmetry	monoclinic	
space group	*C*2/*c*	
Z	8	
a (Å)	4.9824(53)	5.0303(26)
b (Å)	8.7607(39)	8.7268(09)
c (Å)	9.8489(67)	9.8319(32)
β (deg)	99.96(47)	99.79(69)
volume (Å^3)	423.4	425.3
R_p (%)	4.89	4.42
R_{wp} (%)	6.30	5.61
χ^2 (%)	1.79	1.83

Table 2. Calculated Bond Valence Sums (BVSs) of Li_2RuO_3 and $Li_2Ru_{0.75}Ti_{0.25}O_3$ Cathodes

atom	ideal oxidation state	Li_2RuO_3 calculated BVS	$Li_2Ru_{0.75}Ti_{0.25}O_3$ calculated BVS
Ru or Ru/Ti	4	3.43	3.81
Li1	1	1.26	1.32
Li2	1	1.46	1.12
Li3	1	1.12	1.10
Li4	1	1.21	1.09
O1	2	1.70	2.06
O2	2	1.59	1.89
O3	2	2.49	2.18

Figure 3 shows the SEM and TEM images of $Li_2Ru_{0.75}Sn_{0.25}O_3$ and $Li_2Ru_{0.75}Ti_{0.25}O_3$. The particles are well crystallized with a narrow size distribution in the range of 1−1.5 μm. The high magnification SEM image reveals that both compounds consist of a hierarchical assembly of primary nanoparticles to form the micron-sized secondary particles. The morphology was retained irrespective of metal dopant in Li_2RuO_3.

Electrochemical Performance. Figure 4a,b shows the voltage profiles of $Li_2Ru_{0.75}Sn_{0.25}O_3$ and $Li_2Ru_{0.75}Ti_{0.25}O_3$, respectively, at a current density of 14.3 mA g^{-1} (1C = 215 mA g^{-1}) in 2.0−4.8 V vs Li^+/Li for 100 cycles. The first charge profile of the electrodes shows two distinct plateaus, where the first plateau occurs at 3.65 V vs Li^+/Li, corresponding to the redox couple of $Ru^{4+/5+}$, while second plateau > 4.0 V (4.1−4.3 V) is ascribed to the extraction of Li^+ by the anion redox reaction in the form of peroxo-/superoxo-like species as reported for the layered Li_2RuO_3 cathodes. The formation of peroxo-like species is associated with the strong distortion of the oxygen network and the absence of long-range order.[23] The first discharge profile involves a single step redox process occurring at 3.4 V ascribed to the insertion/extraction in $Li_2Ru_{0.75}Ti(/Sn)_{0.25}O_3$. A similar voltage profile was observed

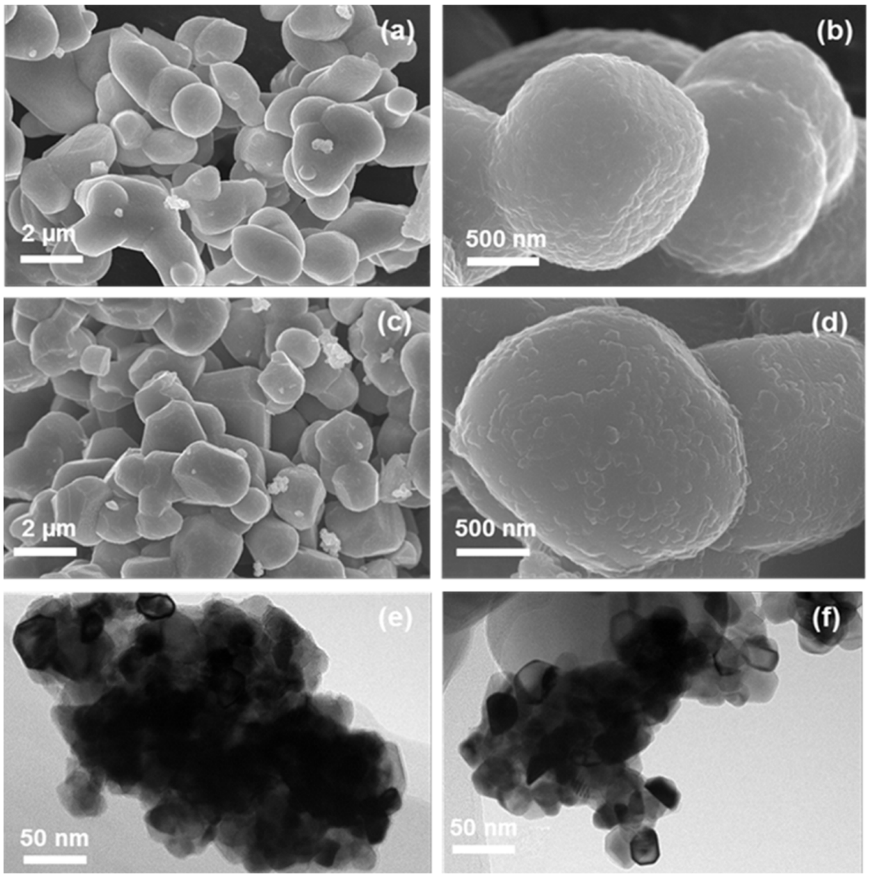

Figure 3. SEM images of (a, b) $Li_2Ru_{0.75}Sn_{0.25}O_3$ and (c, d) $Li_2Ru_{0.75}Ti_{0.25}O_3$ and TEM images of (e) $Li_2Ru_{0.75}Ti_{0.25}O_3$ and (f) $Li_2Ru_{0.75}Sn_{0.25}O_3$.

for subsequent discharge cycles up to 100 cycles. The number of moles of lithium in the first discharging cycle for $Li_2Ru_{0.75}Ti_{0.25}O_3$ was about 1.45 mol of Li^+ as compared to $Li_2Ru_{0.75}Sn_{0.25}O_3$ (1.58 mol of Li^+). However, the number of reversible Li^+ moles after 100 cycles decreased to 1.33 and 1.34 for $Li_2Ru_{0.75}Ti_{0.25}O_3$ and $Li_2Ru_{0.75}Sn_{0.25}O_3$, respectively, as depicted in Figure 4a,b. The Li^+ loss upon cycling for $Li_2Ru_{0.75}Sn_{0.25}O_3$ was too high (0.24 mol of Li^+) than $Li_2Ru_{0.75}Ti_{0.25}O_3$ (0.12 mol of lithium). This reveals that the lithium insertion/extraction occurs more reversibly in $Li_2Ru_{0.75}Ti_{0.25}O_3$ upon cycling that favors long cycle life and improved energy density. Hence, high reversible lithium extraction observed in the $Li_2Ru_{0.75}Ti_{0.25}O_3$ cathode is attributed to the influence of Ti^{4+} on the electrochemical properties of Li_2MO_3 structures.

The robustness of $Li_2Ru_{0.75}Ti_{0.25}O_3$ and $Li_2Ru_{0.75}Sn_{0.25}O_3$ cathodes was tested at high current density (143 mA g^{-1}) and compared with that of pristine Li_2RuO_3, as shown in Figure 4c. The first discharge capacity of pristine Li_2RuO_3 (255 mAh g^{-1}, 1.55 Li^+ moles) was slightly higher than that of $Li_2Ru_{0.75}Ti_{0.25}O_3$ (236 mAh g^{-1}, 1.32 Li^+ moles); however, the capacities of Li_2RuO_3 and $Li_2Ru_{0.75}Sn_{0.25}O_3$ exhibit a rapid decrease in the capacity within ~50 cycles. On the other hand, the discharge capacity of $Li_2Ru_{0.75}Ti_{0.25}O_3$ decreased slightly for the initial few cycles and then increased gradually for about 125 cycles, revealing that the cathode has good electrochemical stability and a high degree of reversibility. The increase in the capacity after a few cycles may be attributed to the electro-activation process induced improvement in the Li-ion diffusion kinetics. Electro-activation of $Li_2Ru_{0.75}Ti_{0.25}O_3$ cathodes was observed up to 125 cycles, and then capacity starts to fade gradually with a final capacity of 172 mAh g^{-1} after 250 cycles. The reversible lithium extraction after 250 cycles was shown to be higher for $Li_2Ru_{0.75}Ti_{0.25}O_3$ (0.96 mol of Li) as compared to pristine (0.79 mol of Li) and $Li_2Ru_{0.75}Sn_{0.25}O_3$ (0.74 mol of Li). High reversible extraction of lithium and excellent cycle life were the attributes of $Li_2Ru_{0.75}Ti_{0.25}O_3$ due to the structural stability of the Li_2RuO_3 structure in the presence of Ti^{4+} species. The electrochemical performance of $Li_2Ru_{1-x}Ti_xO_3$ (x = 0−1.00) series, with varying x value, was also evaluated at a current density of 143 mA g^{-1} and is depicted as Figure S2 (Supporting Information), where the highest electrochemical performance was found with composition, x = 0.25.

The charge/discharge profiles of these cathodes were measured at low current density (14.3 mA g^{-1}) as shown in Figure 4d. The first discharge capacities of $Li_2Ru_{0.75}Sn_{0.25}O_3$ and $Li_2Ru_{0.75}Ti_{0.25}O_3$ were 254 (1.58 mol of Li^+) and 261 mAh g^{-1} (1.45 mol of Li^+), respectively. The $Li_2Ru_{0.75}Sn_{0.25}O_3$ cathodes exhibit gradual fading of the capacity up to 50 cycles. The capacity retention of $Li_2Ru_{0.75}Ti_{0.25}O_3$ at 14.3 mA g^{-1} was quite similar to that of the Sn counterpart with 92% and 85%, respectively. Although both the cathodes have similar electrochemical performance at low discharge rate (14.3 mA g^{-1}), the Ti-based cathodes exhibit excellent performance at high discharge rate, revealing high power capability and long cycle life of the cathode. Recently, Sathiya et al.[26] have reported poor cycle stability for $Li_2Ru_{0.75}Ti_{0.25}O_3$ compared to Li_2RuO_3 and $Li_2Ru_{0.75}Sn_{0.25}O_3$ at low current density (C/5 rate). The cycle performance in the present study, in fact, shows that the discharge capacities and cycle stabilities of $Li_2Ru_{0.75}Ti_{0.25}O_3$ and

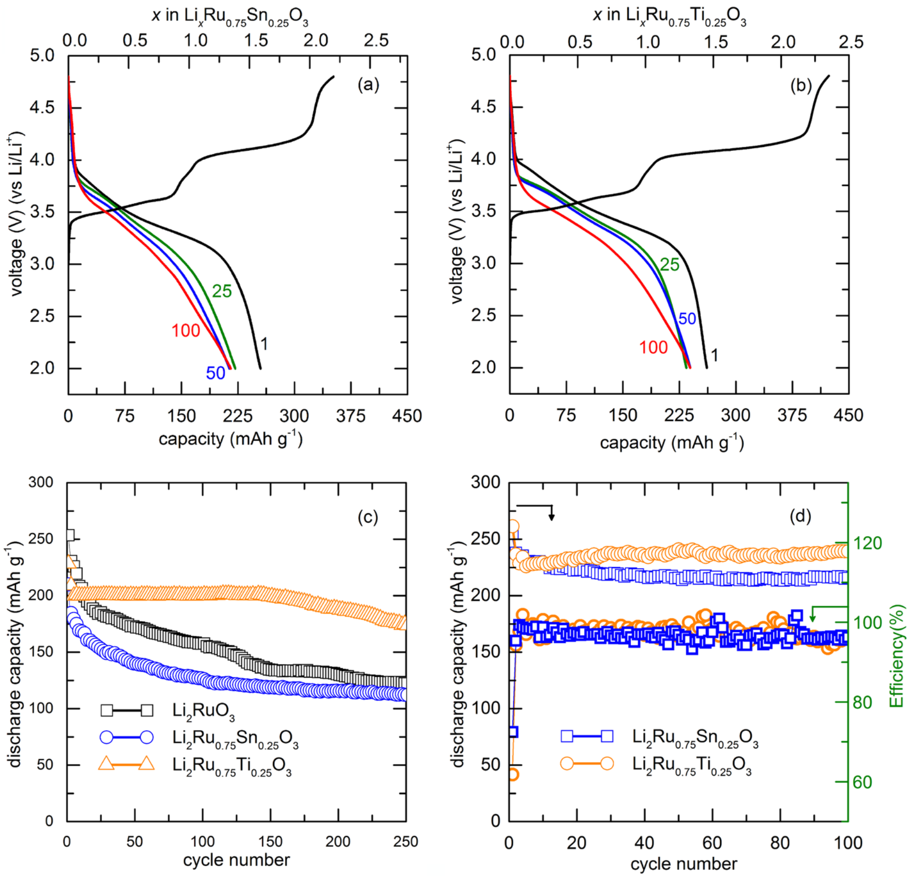

Figure 4. Voltage profiles of (a) $Li_2Ru_{0.75}Sn_{0.25}O_3$ and (b) $Li_2Ru_{0.75}Ti_{0.25}O_3$ cathodes under a current density of 14.3 mA g^{-1} with 100 cycles. (c) Cycling stability curves of Li_2RuO_3, $Li_2Ru_{0.75}Sn_{0.25}O_3$, and $Li_2Ru_{0.75}Ti_{0.25}O_3$ samples at a current density of 143 mA g^{-1}, and (d) cycling stability curves of $Li_2Ru_{0.75}Sn_{0.25}O_3$ and $Li_2Ru_{0.75}Ti_{0.25}O_3$, at a current density of 14.3 mA g^{-1}.

$Li_2Ru_{0.75}Sn_{0.25}O_3$ at low current density (14.3 mA g^{-1}; C/15 rate) are closely in agreement with the report of Sathiya et al.[26] More importantly, the present study demonstrates that excellent cycle stability of $Li_2Ru_{0.75}Ti_{0.25}O_3$ is displayed at a higher current density of 143 mA g^{-1} (0.7C), as seen from Figure 4c. It is highly possible that Sathiya et al.[26] measured the electrochemical performance at lower C rates (C/5 rate) and hence may have showed lower cycle stability. Moreover, a variety of factors including the synthesis temperature, the ratio of electrode fabrication, and method of electrode fabrication may complicate the efforts to provide a comparative report on the electrochemical performance of samples prepared by different groups. For instance, one important factor that influences the electrochemical performance is the synthesis temperature of the cathode, since particle crystallinity influences the electrode properties. In the current study, a higher synthesis temperature was used (1100 °C) compared to that in the report of Sathiya et al.[26] (800 °C). These may be the probable reasons for the difference in electrochemical performance and cycle stability of $Li_2Ru_{0.75}Ti_{0.25}O_3$ over $Li_2Ru_{0.75}Sn_{0.25}O_3$ and Li_2RuO_3 cathodes with respect to Sathiya et al.'s[26] report.

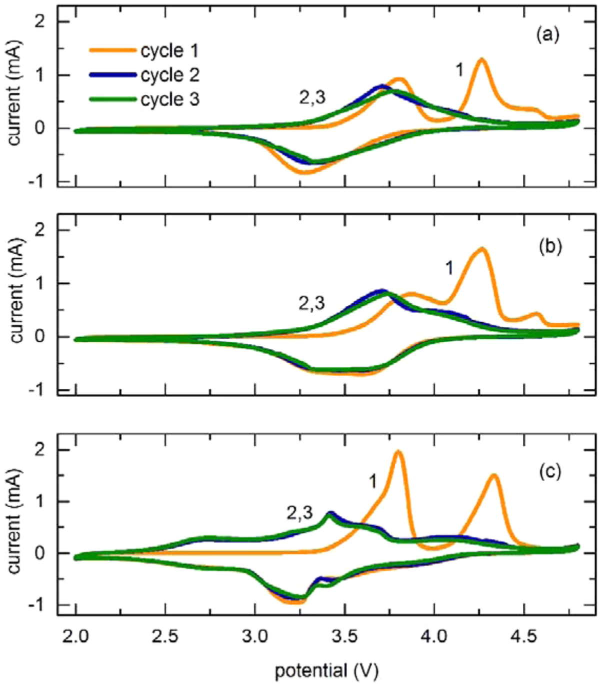

Figure 5. Cyclic voltammogram of (a) $Li_2Ru_{0.75}Sn_{0.25}O_3$, (b) $Li_2Ru_{0.75}Ti_{0.25}O_3$, and (c) Li_2RuO_3 cathodes in the potential window of 2.0−4.8 V at a scan rate of 0.1 mV s^{-1}.

The electrochemical reversibility was studied from the cyclic voltammogram (CV) of the cathodes and is depicted in Figure 5. The first cycle of CV for Li_2RuO_3 (Figure 5c) exhibits a broader oxidation peak ranging from 3.6 to 3.9 V, attributed to the oxidation of Ru^{4+} during Li^+ extraction (~3.65 V) and associated competitive redox mechanism. While similar broader

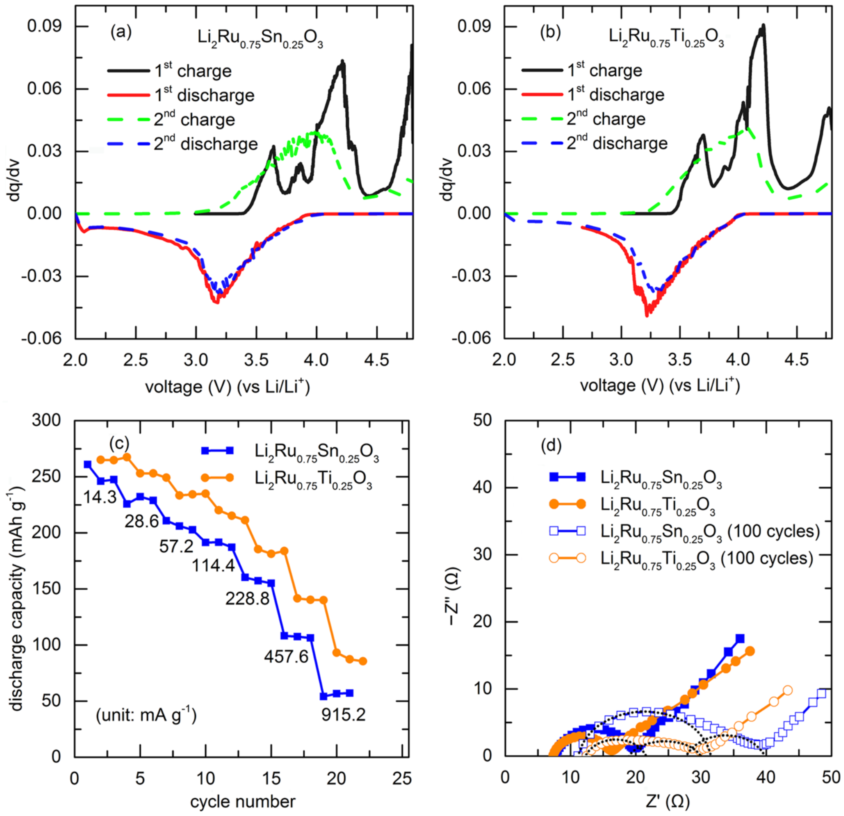

Figure 6. d*q*/d*V* plot of 1st and 2nd charge/discharge cycles of (a) $Li_2Ru_{0.75}Sn_{0.25}O_3$ and (b) $Li_2Ru_{0.75}Ti_{0.25}O_3$ at a current rate of 14.3 mA g^{-1}. (c) Rate capabilities of $Li_2Ru_{0.75}Sn_{0.25}O_3$ and $Li_2Ru_{0.75}Ti_{0.25}O_3$ under different current densities cycled in the potential window of 2.0−4.8 V. (d) Electrochemical impedance spectra of $Li_2Ru_{0.75}Sn_{0.25}O_3$ and $Li_2Ru_{0.75}Ti_{0.25}O_3$ cathodes before and after 100 charge/discharge cycles at a current rate of 14.3 mA g^{-1}.

oxidation peaks at ∼4.2 V (ranging 4.0−4.4 V) are ascribed to the formation of peroxo-/superoxo-like species. The current intensity of the ∼4.2 V peak is prominent in the doped Li_2RuO_3 than the pristine Li_2RuO_3 cathode due to the presence of electroinactive dopant species that increase the formation of peroxo-like species. A minor oxidation peak > 4.5 V may possibly be due to the partial decomposition of carbonate electrolyte. The oxidation of Ru^{4+} in the $Li_2Ru_{0.75}Ti_{0.25}O_3$ cathode occurs at relative higher potential than Li_2RuO_3 and $Li_2Ru_{0.75}Sn_{0.25}O_3$. The oxidation peak due to peroxo-like species (>4.0 V) in the subsequent cycles is retained for the $Li_2Ru_{0.75}Ti_{0.25}O_3$ and pristine electrode, while a negligible peak is observed for the $Li_2Ru_{0.75}Sn_{0.25}O_3$ cathode. The broad reduction peak ranging from 3.1 to 4.3 V is due to the $Ru^{4+/5+}$ redox couple. The two discharge profiles reveal the insertion of lithium and associated reduction of Ru^{5+} to Ru^{4+} species at potential ∼ 3.2 V.

To confirm the electrochemical behavior of the cathode materials, a plot of d*q*/d*V* vs potential (2.0−4.8 V) range was investigated for $Li_2Ru_{0.75}Sn_{0.25}O_3$ and $Li_2Ru_{0.75}Ti_{0.25}O_3$ as shown in Figure 6a,b, respectively. This plot shows the redox processes developed during cycling of electrodes and both the electrodes exhibit similar plots. In the first charging, Ru^{4+} was oxidized to Ru^{5+} during Li^+ extraction, which occurs at a potential of ∼3.65 V. Since further oxidation of Ru^{5+} was not possible, the delithiation is supported by the anion redox reaction in the form of peroxo-/superoxo-like species from the lattice at potential ≥ 4.0 V (4.0−4.4 V) vs Li^+/Li, as reported for the Li_2RuO_3-based layered cathodes.[23] The formation of peroxo-/superoxo-like species at the end of the first charging cycle is attributed to the lithium extraction in association with strong distortion of the oxygen network, by shortening of the O−O bond distance causing an absence of long-range order.[23] The typical peak at ∼3.75 V in the first charging cycle corresponds to the extraction of lithium that follows a single step process. However, the peak intensity of $Li_2Ru_{0.75}Ti_{0.25}O_3$ was weak compared to that of the Sn counterpart. The broad reduction peak ranging from 3.1 to 4.3 V is attributed to the $Ru^{4+/5+}$ redox couple and associated insertion of lithium at ∼3.2 V and corroborates with the CV results (Figure 5).

The rate performance of $Li_2Ru_{0.75}Sn_{0.25}O_3$ and $Li_2Ru_{0.75}Ti_{0.25}O_3$ electrodes under different current densities in the potential range of 2.0−4.8 V at room temperature was tested and is presented in Figure 6c. The discharge capacity of $Li_2Ru_{0.75}Ti_{0.25}O_3$ at a current density of 14.3 mA g^{-1} was 264 mAh g^{-1} and that for $Li_2Ru_{0.75}Sn_{0.25}O_3$ was 247 mAh g^{-1}. However, the capacity decreased with the increase in applied current density. The $Li_2Ru_{0.75}Ti_{0.25}O_3$ cathode retains a capacity of 87 mAh g^{-1} at a higher current density of 915.2 mA g^{-1}, while the $Li_2Ru_{0.75}Sn_{0.25}O_3$ sample could deliver only 56 mAh g^{-1}. The difference in the capacity between these two electrodes at lower current rate (14.3 mA g^{-1}) was minimal, while phenomenal difference was observed at high current rate (915.2 mA g^{-1}) with higher capacity for $Li_2Ru_{0.75}Ti_{0.25}O_3$ cathodes. For a cathode material to deliver high power capability, the electronic conductivity and Li^+ ion mobility in the materials must be high.[39] Hence, the possible reason for higher power capability of $Li_2Ru_{0.75}Ti_{0.25}O_3$ cathodes may be attributed to the structural stability and improved stacking of the Li*M*$_2$ layers, which might lead to the enhanced Li-ion

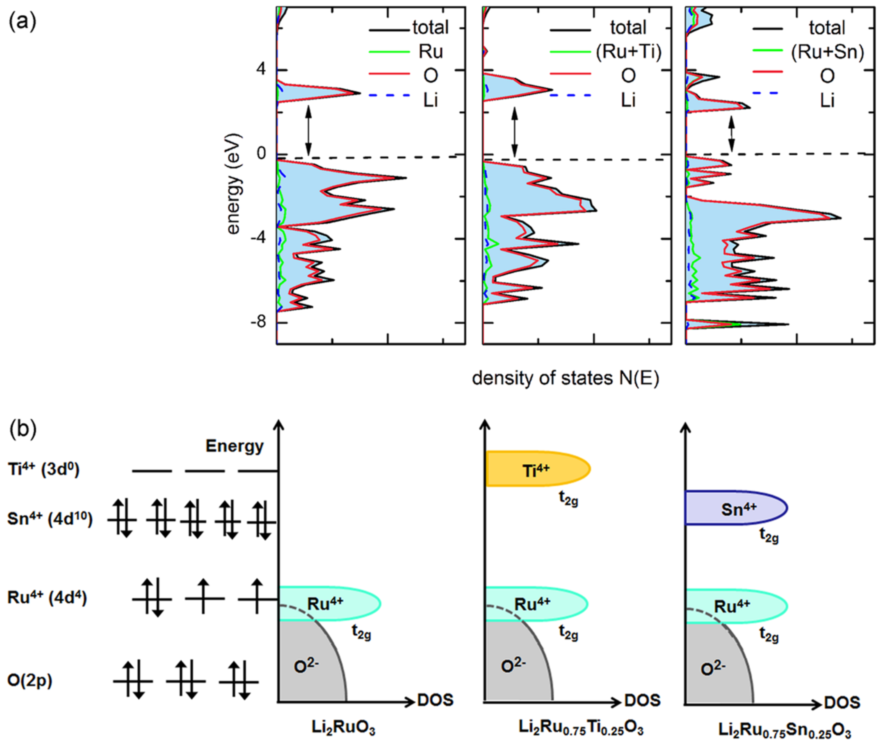

Figure 7. (a) Density of states of Li_2MO_3 with $M = Ru_{0.75}Ti_{0.25}$ (RuTi), Ru (Ru), and $Ru_{0.75}Sn_{0.25}$ (RuSn). Each plot with a black curve depicts total electron density, while green, red, and dotted blue curves depict the partial density of transition metal, oxygen, and lithium, respectively. The dotted black lines indicate the Fermi level, and band gaps are shown by double-headed arrows. (b) Schematic representation of the density of states (DOS) of Li_2RuO_3, $Li_2Ru_{0.75}Ti_{0.25}O_3$, and $Li_2Ru_{0.75}Sn_{0.25}O_3$. The atomic Ti^{4+} 3d, Sn^{4+} 4d, Ru^{4+} 4d, and O^{2-} 2p energy levels are shown to illustrate the lesser electropositive character of Ru and Sn compared to Ti and the stronger Ru (4d)−O (2p) hybridization compared to Ti (3d)−O (2p) and Sn(4d)−O (2p).

diffusion kinetics. Therefore, Ti doping can effectively improve the electrochemical performance of Li_2RuO_3 cathodes in regard to the power capability, cyclability, and discharge capacity. The voltage profile plot of cathodes at different current densities are also depicted in Figure S3 (Supporting Information), which shows the gradual decrease in the capacity for both $Li_2Ru_{0.75}Sn_{0.25}O_3$ and $Li_2Ru_{0.75}Ti_{0.25}O_3$ cathodes at high current densities.

The electrochemical behavior of these electrodes was further investigated using electrochemical impedance spectroscopy (EIS) before and after 100 cycles at 14.3 mA g^{-1} and are shown in Figure 6d. The charge-transfer resistance (R_{ct}) and double-layer capacitance (C_{dl}) across the electrode/electrolyte interface is depicted by the high frequency semicircle, while, at low frequency, the diffusion of lithium in the bulk active mass was observed.[7] The semicircle in the high frequency domain reveals a typical Randle's circuit equivalent circuit where resistance and capacitance/constant phase element connected in parallel fashion. The charge-transfer resistance of $Li_2Ru_{0.75}Ti_{0.25}O_3$ before cycling was low with 8.6 Ω compared to 11.6 Ω for $Li_2Ru_{0.75}Sn_{0.25}O_3$ cathodes. After 100 cycles, there were slight changes in the impedance spectra of both the electrodes, where two semicircles merged together at high and intermediate frequency and Warburg diffusion (linear line) was observed at the lower frequency domain. An increase in the diameter of the merged semicircles (shown as dotted curves in Figure 6d) reveals an enhanced overall charge-transfer resistance of the cell, which fits with two Randel's circuits (resistance and capacitance/constant phase element in parallel) in series. The first semicircle corresponds to the resistance of the solid electrolyte interface (SEI) film that constitutes a series of spontaneous reactions between the cathode material and electrolyte solvent at high operating voltage.[40,41] The second semicircle at intermediate frequency is ascribed to the charge-transfer resistance due to the lithium intercalation/deintercalation process.[40] After 100 cycles, the SEI film resistance of the $Li_2Ru_{0.75}Ti_{0.25}O_3$ electrode increased to 10.0 Ω as compared to that of the Sn-doped counterpart, which increased to 20.0 Ω. The charge-transfer resistances of $Li_2Ru_{0.75}Ti_{0.25}O_3$ and $Li_2Ru_{0.75}Sn_{0.25}O_3$ electrodes are 7.0 and 8.0 Ω, respectively. The increase in the SEI resistance upon cycling is due to the growth of the passivating SEI film on the electrode caused by the partial oxidation of electrolyte at high operating voltage. However, the overall resistance of $Li_2Ru_{0.75}Ti_{0.25}O_3$ electrodes after 100 cycles is lower (17.0 Ω) compared to that of the Sn-doped counterpart (28.0 Ω). In fact, the total resistance influences the electrochemical performance, namely, the specific capacity and cycle life of the electrode in Li-ion battery applications.

Impedance spectra of $Li_2Ru_{0.75}M_{0.25}O_3$ (M = Sn, Ti) and Li_2RuO_3 cathodes at different states of charge, namely, charged to 4.0, 4.8, and discharged at 2.0 V, are presented in Figure S4 (Supporting Information), and the corresponding charge-transfer resistance (R_{ct}) components are tabulated in Table S2 (Supporting Information). Most of the impedance spectra show a single semicircle revealing the typical Randle's circuit with resistance and capacitance in parellel. The impedance of the cathode charged at 4.0 V reveals that the charge-transfer resistance of $Li_2Ru_{0.75}Ti_{0.25}O_3$ and Li_2RuO_3 (~25.0 Ω) are similar, while $Li_2Ru_{0.75}Sn_{0.25}O_3$ showed higher resistance

(~30.0 Ω). The R_{ct} of Li_2RuO_3 charged at 4.8 V was the lowest (~35.0 Ω) with the formation of metallic RuO_x (E_g = ≤2.2 eV as for RuO_2), while $Li_2Ru_{0.75}Ti_{0.25}O_3$ showed slightly higher R_{ct} (~37 Ω) due to the formation of $Ru_{1-x}Ti_xO_2$ with the semiconducting component, TiO_2 (E_g = 3.2 eV) and metallic RuO_x. The resistance was the highest for $Li_2Ru_{0.75}Sn_{0.25}O_3$ (~62.0 Ω) due to the formation of high band gap semiconductor SnO_2 (E_g = 3.8 eV) and metallic RuO_x. On subsequent discharge to 2.0 V, the structure nearly comes back to the pristine layered structure, and the observed R_{ct} was retained with that of the cathode before electrochemical cycling (as shown in Figure 6d). However, the R_{ct} of $Li_2Ru_{0.75}Ti_{0.25}O_3$ was the lowest with ~17.0 Ω, while $Li_2Ru_{0.75}Sn_{0.25}O_3$ showed relatively higher R_{ct} with ~26.0 Ω. The impedance spectra of Li_2RuO_3 discharged at 2.0 V is split into two semicircles where the first semicircle corresponds to the resistance of the SEI film layer with ~10.0 Ω, while the second semicircle corresponds to the charge-transfer resistance with ~27.0 Ω, as shown in Figure S4c (Supporting Information). The overall resistance of the Li_2RuO_3 electrode discharged at 2.0 V is larger. Under any of the state of charge, the Ti electrode showed lower charge-transfer resistance, indicating superior electrochemical performance of Ti doping than the Sn counterpart.

The lower charge-transfer resistance and higher conductivity of Ti-doped electrode over Sn may be explained in terms of metal−oxygen bonding nature. The Pauling values of electronegativity for Ru, Sn, and Ti elements are 2.20, 1.96, and 1.54, respectively.[42] RuO_6 exists in the transition metal layer in which Ti and Sn substitute the Ru site with six coordination. Ionic bonding occurs when a large difference in the electronegativity was observed between two bonding atoms. Hence, the bonding between these transition metals and oxygen (electronegativity: 3.44) gives a difference of 1.24, 1.48, and 1.90 for Ru−O, Sn−O, and Ti−O, respectively. The large difference in electronegativity for Ti−O reveals more ionic bond than the Sn−O/Ru−O bond and which realizes a strong interaction between the Ti^{4+} cation and the surrounding counter O^{2-} anions, leading to an improved conductivity. In other words, Sn^{4+} is hard to ionize and more likely to accept electrons than Ti^{4+}. Hence, it is clear that the decrease in charge-transfer resistance is beneficial to the kinetic behaviors during the charge/discharge process. This indicates that Ti doping improves the electronic/ionic conductivity than the Sn couterpart in Li_2RuO_3, since EIS spectra give a combination of both electronic and ionic conductivity components. Therefore, the high power capability and cyclability of $Li_2Ru_{0.75}Ti_{0.25}O_3$ cathodes are attibuted to the lower charge-transfer resistance, as confirmed from the electrochemical results and improved structural rigidity of the LiM_2 layer favoring enhanced lithium diffusion kinetics.

Density Functional Theory Calculations. The electrochemical properties of the electrodes may be well understood by the density of states (DOS) calculation. The DOS diagrams of the Li_2RuO_3 (Ru), $Li_2Ru_{0.75}Sn_{0.25}O_3$ (Ru + Sn), and $Li_2Ru_{0.75}Ti_{0.25}O_3$ (Ru + Ti) are shown in Figure 7a. The band gap of $Li_2Ru_{0.75}Ti_{0.25}O_3$ from DFT calculations is slightly larger (2.8 eV) than that of $Li_2Ru_{0.75}Sn_{0.25}O_3$ (2.0 eV). The DOS of Li_2RuO_3 and doped Li_2RuO_3 electrodes was explored in detail in the previous literatures.[43,44] The schematic electronic band structures of $Li_2Ru_{0.75}M_{0.25}O_3$ (M = Ti and Sn) and pristine Li_2RuO_3 are depicted in Figure 7b. The structures describe a strong hybridization of the 4d band of Ru with the oxygen 2p band. The plot reveals that the Li_2RuO_3 shows that 2/3 sites are filled with a Ru^{4+} (t_{2g}) band in which the four valence electrons are delocalized over the Ru−O and Ru−Ru bonds. In contrast, the $Li_2Ru_{0.75}Ti_{0.25}O_3$ shows the Ti^{4+} (t_{2g}) band in which the d electrons are vacant on the transition metal sites. The band structure reveals that Ti doping marginally increases the band gap energy of Li_2RuO_3 cathodes, which is in agreement with the reported literature from DFT calculations.[6]

Thus, the influence of Ti on the electrochemical performance of Li_2MO_3 (M = Ru) Li-rich layered oxides was understood and reveals that the enhanced electrochemical performance is attributed to lower charge-transfer resistance and facile lithium-ion transport due to structural stability of the LiM_2 layer. The current study would be of significance to the development of high capacity Li-rich layered oxide cathodes with insight on the structural stability of the LiM_2 layer in the presence of electroinactive Ti^{4+} species on the electrochemical performance of the cathodes.

■ CONCLUSIONS

Layered $Li_2Ru_{0.75}Ti_{0.25}O_3$ and $Li_2Ru_{0.75}Sn_{0.25}O_3$ cathodes were synthesized by solid-state reaction. The effect of Ti and Sn doping on the structure and electrochemical properties of Li_2MO_3 (M = Ru) cathodes was investigated. Structural analysis reveals that Ti doping favors superior structural stability in $Li_2Ru_{0.75}Ti_{0.25}O_3$, facilitating better lithium-ion diffusion and improved electronic conductivity in the Li_2RuO_3 structure. $Li_2Ru_{0.75}Sn_{0.25}O_3$ suffers from stacking faults that block the lithium diffusion pathway. High reversible capacity was observed for $Li_2Ru_{0.75}Ti_{0.25}O_3$ at 143 mA g^{-1} (high current rate) with a capacity retention of 72% after 250 cycles compared to Li_2MO_3 (M = Ru, $Ru_{0.75}Sn_{0.25}$) with a retention of <50% in the potential window of 2.0−4.8 V. The improved cyclability and power capability of $Li_2Ru_{0.75}Ti_{0.25}O_3$ cathodes were attributed to high structural stability facilitating lower charge-transfer resistance, lithium diffusion kinetics, and reduced covalent nature of the Ti−O bond. Ti-doped Li_2RuO_3 exhibits excellent rate capability and long cycle life, which would open the gateway for exploiting Ti-based Li_2MO_3 cathodes as promising candidates for electric vehicular applications.

■ ASSOCIATED CONTENT

Ⓢ Supporting Information

X-ray diffraction and electrochemical cycling of $Li_2Ru_{1-x}Ti_xO_3$ cathodes with x = 0, 0.1, 0.25, 0.4, 0.6, 0.8, and 1.0 at 143 mA g^{-1}; voltage profile of $Li_2Ru_{0.75}M_{0.25}O_3$ (M = Sn and Ti) cathodes at different current densities; and electrochemical impedance spectra of Li_2RuO_3 and $Li_2Ru_{0.75}M_{0.25}O_3$ (M = Sn and Ti) cathodes at different state of charge. This material is available free of charge via the Internet at http://pubs.acs.org.

■ AUTHOR INFORMATION

Corresponding Author

*Tel: +82-62-530-1715. Fax: +82-62-530-1699. E-mail: imwonbin@jnu.ac.kr (W.B.I.).

Author Contributions

‖These authors contributed equally.

Notes

The authors declare no competing financial interest.

■ ACKNOWLEDGMENTS

This research was supported by the MKE (The Ministry of Knowledge Economy), Korea, under the ITRC (Information Technology Research Center) support program (NIPA-2013-H0301-13-1009) supervised by the NIPA (National IT Industry Promotion Agency). This research was also supported by the Basic Science Research Program through the National Research Foundation of Korea (NRF), funded by the Ministry of Education, Science and Technology and NRF through the Human Resource Training Project for Regional Innovation.

■ REFERENCES

(1) Tarascon, J. M.; Armand, M. Issues and Challenges Facing Rechargeable Lithium Batteries. *Nature* **2001**, *414*, 359−367.

(2) Thackeray, M. M.; Johnson, C. S.; Vaughey, J. T.; Li, N.; Hackney, S. A. Advances in Manganese-Oxide 'Composite' Electrodes for Lithium-Ion Batteries. *J. Mater. Chem.* **2005**, *15*, 2257−2267.

(3) Hosono, E.; Wang, Y.; Kida, N.; Enomoto, M.; Kojima, N.; Okubo, M.; Matsuda, H.; Saito, Y.; Kudo, T.; Honma, I.; Zhou, H. Synthesis of Triaxial $LiFePO_4$ Nanowire with a VGCF Core Column and a Carbon Shell through the Electrospinning Method. *ACS. Appl. Mater. Interfaces* **2009**, *2*, 212−218.

(4) Feng, J.; Huang, Z.; Guo, C.; Chernova, N. A.; Upreti, S.; Whittingham, M. S. An Organic Coprecipitation Route to Synthesize High Voltage $LiNi_{0.5}Mn_{1.5}O_4$. *ACS. Appl. Mater. Interfaces* **2013**, *5*, 10227−10232.

(5) Kim, Y.; Veith, G. M.; Nanda, J.; Unocic, R. R.; Chi, M.; Dudney, N. J. High Voltage Stability of $LiCoO_2$ Particles with a Nano-scale Lipon Coating. *Electrochim. Acta* **2011**, *56*, 6573−6580.

(6) Zhu, J.; Vo, T.; Li, D.; Lu, R.; Kinsinger, N. M.; Xiong, L.; Yan, Y.; Kisailus, D. Crystal Growth of $Li[Ni_{1/3}Co_{1/3}Mn_{1/3}]O_2$ as a Cathode Material for High-Performance Lithium Ion Batteries. *Cryst. Growth Des.* **2012**, *12*, 1118−1123.

(7) Thackeray, M. M.; Kang, S.-H.; Johnson, C. S.; Vaughey, J. T.; Benedek, R.; Hackney, S. A. Li_2MnO_3-stabilized $LiMO_2$ (M = Mn, Ni, Co) Electrodes for Lithium-Ion Batteries. *J. Mater. Chem.* **2007**, *17*, 3112−3125.

(8) Yu, H.; Zhou, H. High-Energy Cathode Materials (Li_2MnO_3−$LiMO_2$) for Lithium-Ion Batteries. *J. Phys. Chem. Lett.* **2013**, *4*, 1268−1280.

(9) Johnson, C. S.; Li, N.; Lefief, C.; Vaughey, J. T.; Thackeray, M. M. Synthesis, Characterization and Electrochemistry of Lithium Battery Electrodes: $xLi_2MnO_3\cdot(1-x)LiMn_{0.333}Ni_{0.333}Co_{0.333}O_2$ ($0\leq x \leq 0.7$). *Chem. Mater.* **2008**, *20*, 6095−6106.

(10) Numata, K.; Sakaki, C.; Yamanaka, S. Synthesis and Characterization of Layer Structured Solid Solutions in the System of $LiCoO_2$−Li_2MnO_3. *Solid State Ionics* **1999**, *117*, 257−263.

(11) Massarotti, V.; Bini, M.; Capsoni, D.; Altomare, A.; Moliterni, A. G. G. Ab Initio Structure Determination of Li_2MnO_3 from X-ray Powder Diffraction Data. *J. Appl. Crystallogr.* **1997**, *30*, 123−127.

(12) James, A. C. W. P.; Goodenough, J. B. Structure and Bonding in Lithium Ruthenate, Li_2RuO_3. *J. Solid State Chem.* **1988**, *74*, 287−294.

(13) Kataoka, K.; Takahashi, Y.; Kijima, N.; Nagai, H.; Akimoto, J.; Idemoto, Y.; Ohshima, K.-i. Crystal Growth and Structure Refinement of Monoclinic Li_2TiO_3. *Mater. Res. Bull.* **2009**, *44*, 168−172.

(14) Dittrich, G.; Hoppe, R. Die Kristallstruktur von Li_2ZrO_3 und Li_2HfO_3. *Z. Anorg. Allg. Chem.* **1969**, *371*, 306−317.

(15) Jarvis, K. A.; Deng, Z.; Allard, L. F.; Manthiram, A.; Ferreira, P. J. Atomic Structure of a Lithium-Rich Layered Oxide Material for Lithium-Ion Batteries: Evidence of a Solid Solution. *Chem. Mater.* **2011**, *23*, 3614−3621.

(16) Tarakina, N. V.; Denisova, T.; Maksimova, L.; Baklanova, Y.; Tyutyunnik, A.; Berger, I.; Zubkov, V.; Van Tendeloo, G. Investigation of Stacking Disorder in Li_2SnO_3. *Z. Kristallogr.* **2009**, *36*, 37.

(17) Kobayashi, H.; Tabuchi, M.; Shikano, M.; Kageyama, H.; Kanno, R. Structure, and Magnetic and Electrochemical Properties of Layered Oxides, Li_2IrO_3. *J. Mater. Chem.* **2003**, *13*, 957−962.

(18) Todorova, V.; Jansen, M. Synthesis, Structural Characterization and Physical Properties of a New Member of Ternary Lithium Layered Compounds — Li_2RhO_3. *Z. Anorg. Allg. Chem.* **2011**, *637*, 37−40.

(19) Okada, S.; Yamaki, J.-i.; Asakura, K.; Ohtsuka, H.; Arai, H.; Tobishima, S.-i.; Sakurai, Y. Cathode Characteristics of Layered Rocksalt Oxide, Li_2PtO_3. *Electrochim. Acta* **1999**, *45*, 329−334.

(20) Ma, J.; Zhou, Y.-N.; Gao, Y.; Yu, X.; Kong, Q.; Gu, L.; Wang, Z.; Yang, X.-Q.; Chen, L. Feasibility of Using Li_2MoO_3 in Constructing Li-Rich High Energy Density Cathode Materials. *Chem. Mater.* **2014**, *26*, 3256−3262.

(21) Denis, Y.; Yanagida, K.; Kato, Y.; Nakamura, H. Electrochemical Activities in Li_2MnO_3. *J. Electrochem. Soc.* **2009**, *156*, A417−A424.

(22) Denis, Y.; Yanagida, K. Structural Analysis of Li_2MnO_3 and Related Li-Mn-O Materials. *J. Electrochem. Soc.* **2011**, *158*, A1015−A1022.

(23) Sathiya, M.; Rousse, G.; Ramesha, K.; Laisa, C. P.; Vezin, H.; Sougrati, M. T.; Doublet, M.-L.; Foix, D.; Gonbeau, D.; Walker, W.; Prakash, A. S.; Ben Hassine, M.; Dupont, L.; Tarascon, J.-M. Reversible Anionic Redox Chemistry in High-Capacity Layered-Oxide Electrodes. *Nat. Mater.* **2013**, *12*, 827−835.

(24) Kim, J.; Amine, K. A Comparative Study on the Substitution of Divalent, Trivalent and Tetravalent Metal Ions in $LiNi_{1-x}M_xO_2$ (M = Cu^{2+}, Al^{3+} and Ti^{4+}). *J. Power Sources* **2002**, *104*, 33−39.

(25) Myung, S.-T.; Komaba, S.; Hosoya, K.; Hirosaki, N.; Miura, Y.; Kumagai, N. Synthesis of $LiNi_{0.5}Mn_{0.5-x}Ti_xO_2$ by an Emulsion Drying Method and Effect of Ti on Structure and Electrochemical Properties. *Chem. Mater.* **2005**, *17*, 2427−2435.

(26) Sathiya, M.; Abakumov, A. M.; Foix, D.; Rousse, G.; Ramesha, K.; Saubanère, M.; Doublet, M. L.; Vezin, H.; Laisa, C. P.; Prakash, A. S.; Gonbeau, D.; VanTendeloo, G.; Tarascon, J. M. Origin of Voltage Decay in High-Capacity Layered Oxide Electrodes. *Nat. Mater.* **2015**, *14*, 230−238.

(27) Larson, A. C.; Von Dreele, R. B. *General Structure Analysis System (GSAS)*; Los Alamos National Laboratory Report LAUR 86-748; The Regents of the University of California: Oakland, CA, 1994.

(28) Kresse, G.; Furthmüller, J. Efficient Iterative Schemes for *Ab Initio* Total-Energy Calculations Using a Plane-Wave Basis Set. *Phys. Rev. B* **1996**, *54*, 11169−11186.

(29) Perdew, J. P.; Wang, Y. Accurate and Simple Analytic Representation of the Electron-Gas Correlation Energy. *Phys. Rev. B* **1992**, *45*, 13244.

(30) Morgan, B. J.; Watson, G. W. A DFT+U Description of Oxygen Vacancies at the TiO_2 Rutile (110) Surface. *Surf. Sci.* **2007**, *601*, 5034−5041.

(31) Kobayashi, H.; Kanno, R.; Kawamoto, Y.; Tabuchi, M.; Nakamura, O.; Takano, M. Structure and Lithium Deintercalation of $Li_{2-x}RuO_3$. *Solid State Ionics* **1995**, *82*, 25−31.

(32) Shannon, R. Revised Effective Ionic Radii and Systematic Studies of Interatomic Distances in Halides and Chalcogenides. *Acta Crystallogr., Sect. A: Found. Crystallogr.* **1976**, *32*, 751−767.

(33) Bréger, J.; Jiang, M.; Dupré, N.; Meng, Y. S.; Shao-Horn, Y.; Ceder, G.; Grey, C. P. High-Resolution X-ray Diffraction, DIFFaX, NMR and First Principles Study of Disorder in the Li_2MnO_3−$Li[Ni_{1/2}Mn_{1/2}]O_2$ Solid Solution. *J. Solid State Chem.* **2005**, *178*, 2575−2585.

(34) Wang, R.; He, X.; He, L.; Wang, F.; Xiao, R.; Gu, L.; Li, H.; Chen, L. Atomic Structure of Li_2MnO_3 after Partial Delithiation and Re-Lithiation. *Adv. Energy Mater.* **2013**, *3*, 1358−1367.

(35) Meng, Y.; Ceder, G.; Grey, C.; Yoon, W.-S.; Jiang, M.; Breger, J.; Shao-Horn, Y. Cation Ordering in Layered O3 $Li[Ni_xLi_{1/3-2x/3}Mn_{2/3-x/3}]O_2$ ($0\leq x \leq 1/2$) Compounds. *Chem. Mater.* **2005**, *17*, 2386−2394.

(36) Sivasekar, S.; Ramalingam, K.; Rizzoli, C.; Alexander, N. Synthesis, Structural, Continuous Shape Measure and Bond Valence Sum Characterization of Bismuth(III) Complexes of Substituted Dithiocarbamates and Their Solvothermal Decomposition. *Inorg. Chim. Acta* **2014**, *419*, 82−88.

(37) Denault, K. A.; Brgoch, J.; Gaultois, M. W.; Mikhailovsky, A.; Petry, R.; Winkler, H.; DenBaars, S. P.; Seshadri, R. Consequences of

Optimal Bond Valence on Structural Rigidity and Improved Luminescence Properties in $Sr_xBa_{2-x}SiO_4$:Eu^{2+} Orthosilicate Phosphors. *Chem. Mater.* **2014**, *26*, 2275−2282.

(38) Yoon, W.-S.; Iannopollo, S.; Grey, C. P.; Carlier, D.; Gorman, J.; Reed, J.; Ceder, G. Local Structure and Cation Ordering in O3 Lithium Nickel Manganese Oxides with Stoichiometry $Li[Ni_xMn_{(2-x)/3}Li_{(1-2x)/3}]O_2$ NMR Studies and First Principles Calculations. *Electrochem. Solid-State Lett.* **2004**, *7*, A167−A171.

(39) Linden, D., Reddy, T. B., Eds. *Handbook of Batteries*, 3rd ed.; McGraw-Hill Pub.: New York, 2002; Chapter 35, pp 35.1−35.6.

(40) Fu, C.; Li, G.; Luo, D.; Li, Q.; Fan, J.; Li, L. Nickel-Rich Layered Microspheres Cathodes: Lithium/Nickel Disordering and Electrochemical Performance. *ACS. Appl. Mater. Interfaces* **2014**, *6*, 15822−15831.

(41) Choi, N.-S.; Han, J.-G.; Ha, S.-Y.; Park, I.; Back, C.-K. Recent Advances in the Electrolytes for Interfacial Stability of High-Voltage Cathodes in Lithium-Ion Batteries. *RSC Adv.* **2015**, *5*, 2732−2748.

(42) Pauling, L. *The Nature of the Chemical Bond and the Structure of Molecules and Crystals: An Introduction to Modern Structural Chemistry*; Cornell University Press: Ithaca, NY, 1960; Vol. *18*.

(43) Sarkar, S.; Mahale, P.; Mitra, S. Lithium Rich Composition of Li_2RuO_3 and $Li_2Ru_{1-x}Ir_xO_3$ Layered Materials as Li-Ion Battery Cathode. *J. Electrochem. Soc.* **2014**, *161*, A934−A942.

(44) Sathiya, M.; Ramesha, K.; Rousse, G.; Foix, D.; Gonbeau, D.; Prakash, A. S.; Doublet, M. L.; Hemalatha, K.; Tarascon, J. M. High Performance $Li_2Ru_{1-y}Mn_yO_3$ ($0.2 \leq y \leq 0.8$) Cathode Materials for Rechargeable Lithium-Ion Batteries: Their Understanding. *Chem. Mater.* **2013**, *25*, 1121−1131.